Diagnostic Study

INTERNATIONAL JOURNAL OF SURGERY

OPEN

Computed tomography-based fully automated artificial intelligence model to predict extrapancreatic perineural invasion in pancreatic ductal adenocarcinoma

Jieyu Yu, MS[a], Chengwei Chen, MD, PhD[a], Mingzhi Lu, MS[b], Xu Fang, MS[a], Jing Li, MD, PhD[a], Mengmeng Zhu, MS[a], Na Li, MS[a], Xiaohan Yuan, MD, PhD[a], Yaxing Han, MS[c], Li Wang, MD, PhD[a], Jianping Lu, MD, PhD[a], Chengwei Shao, MD, PhD[a,*], Yun Bian, MD, PhD[a,*]

Background: Extrapancreatic perineural invasion (EPNI) increases the risk of postoperative recurrence in pancreatic ductal adenocarcinoma (PDAC). This study aimed to develop and validate a computed tomography (CT)-based, fully automated preoperative artificial intelligence (AI) model to predict EPNI in patients with PDAC.

Methods: The authors retrospectively enrolled 1065 patients from two Shanghai hospitals between June 2014 and April 2023. Patients were split into training ($n = 497$), internal validation ($n = 212$), internal test ($n = 180$), and external test ($n = 176$) sets. The AI model used perivascular space and tumor contact for EPNI detection. The authors evaluated the AI model's performance based on its discrimination. Kaplan–Meier curves, log-rank tests, and Cox regression were used for survival analysis.

Results: The AI model demonstrated superior diagnostic performance for EPNI with 1-pixel expansion. The area under the curve in the training, validation, internal test, and external test sets were 0.87, 0.88, 0.82, and 0.83, respectively. The log-rank test revealed a significantly longer survival in the AI-predicted EPNI-negative group than the AI-predicted EPNI-positive group in the training, validation, and internal test sets ($P < 0.05$). Moreover, the AI model exhibited exceptional prognostic stratification in early PDAC and improved assessment of neoadjuvant therapy's effectiveness.

Conclusion: The AI model presents a robust modality for EPNI diagnosis, risk stratification, and neoadjuvant treatment guidance in PDAC, and can be applied to guide personalized precision therapy.

Keywords: Artificial intelligence, carcinoma, multidetector computed tomography, pancreatic ductal, perineural, survival

Introduction

Pancreatic ductal adenocarcinoma (PDAC) is a leading cause of cancer-related deaths, projected to rank second globally by 2030[1]. Although surgery with adjuvant chemotherapy remains the only potentially curative option, cancer recurs in up to 80% of patients, mostly within 2 years after operation[2]. A significant factor contributing to this is extrapancreatic perineural invasion (EPNI), observed in 52.2–75.8% of surgical specimens, leading to early recurrence and poor prognosis[3–5].

The peripancreatic nerve plexus, intertwined with major blood vessels like the celiac artery (CA) and its branches, portal vein (PV), superior mesenteric artery (SMA), and splenic artery (SA), is

HIGHLIGHTS

- We identified a critical area using computed tomography (CT) based on deep learning—the perivascular space, highlighting a novel area for diagnosing extrapancreatic perineural invasion (EPNI) in pancreatic cancer.
- A fully automatic artificial intelligence (AI) model was developed and validated, demonstrating good performance across multiple centers for diagnosing EPNI in pancreatic ductal adenocarcinoma (PDAC).
- The risk stratification of the AI-predicted EPNI had substantial associations with the overall survival (OS) of patients, adding value to the prognostic stratification of pathological TNM staging systems.
- The AI-predicted EPNI could improve assessment of neoadjuvant therapy (NAT)'s effectiveness, combining with RECIST 1.1 scores and TRG grading.

[a]Department of Radiology, Changhai Hospital, [b]Department of Oncology Radiation, Changhai Hospital and [c]Department of Radiology, No. 411 Hospital, Shanghai, China

J.Y., C.C., and M.L. contributed equally to this work.

Sponsorships or competing interests that may be relevant to content are disclosed at the end of this article.

*Corresponding author. Address: Department of Radiology, Changhai Hospital, Shanghai 200433, China. Tel: +86 133 862 741 78; fax: +86 311 62176. E-mail: chengweishaoch@163.com (C. Shao), and Tel.: +86 138 163 57024. E-mail: bianyun2012@foxmail.com (Y. Bian).

International Journal of Surgery (2024) 110:7656–7670

Received 11 March 2024; Accepted 29 April 2024

Supplemental Digital Content is available for this article. Direct URL citations are provided in the HTML and PDF versions of this article on the journal's website, www.lww.com/international-journal-of-surgery.

Published online 13 May 2024

http://dx.doi.org/10.1097/JS9.0000000000001604

a common pathway for tumor spread[6–8]. This complexity complicates complete surgical resection, often resulting in positive surgical margins. Several retrospective studies have demonstrated that extended resection effectively prolongs the overall survival time of patients[9–11]. However, successive randomized controlled trials in Europe and the United States have indicated that compared to standard radical resection, extended radical resection of pancreatic cancer does not improve long-term patient prognosis and increases complications such as diarrhea and malnutrition[12,13]. Hence, accurate EPNI diagnosis is crucial to tailor surgical interventions, minimize postoperative recurrence, and enhance long-term survival.

Computed tomography (CT) has been employed for the preoperative evaluation of EPNI in pancreatic cancer[8]. A retrospective study by Chang *et al.*[14] demonstrated that hypoattenuating tumors infiltrating the SMA, posterior inferior pancreaticoduodenal artery (PIPDA), and common hepatic artery (CHA) are reliable imaging features for EPNI. Similarly, Khristenko *et al.*[15] reported that perivascular soft tissue infiltration and contact with the tumor are dependable signs of EPNI. Therefore, previous research on explanations for EPNI has focused on the direct observation of microstructures, and thus lacks objective standards. Moreover, other conditions, such as fibrosis and inflammation around blood vessels, can mimic perineural invasion, resulting in a moderate specificity of 64.7% for traditional features[15]. These drawbacks limit the clinical utility of CT for assessing EPNI and necessitate the use of more reliable diagnostic methodologies.

However, as research advanced, it became clear[16,17] that PNI results from interactions between cancer cells and the nerve microenvironment. The spatial gap between the nerve plexus and tumor plays a critical role in nerve growth, tumor proliferation, and perineural invasion. Recognizing the intimate anatomical relationship between the nerve plexus and blood vessels, we identified the perivascular space as key for EPNI. With the widespread implementation of deep-learning (DL) segmentation tools, the automated segmentation of tumors and blood vessels has emerged as a feasible approach[18,19]. In our study, we utilized a DL algorithm for the automatic segmentation of tumors and peripheral blood vessels. We then expanded the vessel contours to delineate perivascular spaces where the nerve plexus existed. We then evaluated the interaction between the tumor and the perivascular space to simulate tumor infiltration into the nerve plexus. This objective measurement served as the output of our final model, overcoming the traditional imaging limitations for the diagnosis of EPNI and making the diagnosis of pancreatic cancer using EPNI feasible.

Methods

Study design and patients

This study fundamentally followed the STARD[20] guidelines, Supplemental Digital Content 1, http://links.lww.com/JS9/C500 and TRIPOD[21] guidelines for individual prognosis or diagnosis. Data were obtained from consecutively diagnosed individuals attending two participating hospitals (Changhai Hospital and NO. 411 Hospital). The study was approved by the Institutional Ethics Review Board of the two medical centers and conducted in accordance with the Declaration of Helsinki. The requirement for informed consent was waived by the institutional review board because of the retrospective nature of the study and because all procedures were performed as part of routine care. In addition, this study was registered at ClinicalTrials.gov (trail number: ChiCTR2000038576). All patients were divided into four datasets: training, validation, internal testing [neoadjuvant therapy (NAT)], and external testing.

In the initial phase, we conducted a retrospective single-center primary cohort study of 889 patients treated at Changhai Hospital between June 2014 and May 2022. Inclusion criteria were: (a) histopathologically confirmed pancreatic ductal adenocarcinoma and (b) pretreatment contrast-enhanced CT scans available within one month before surgery. Exclusion criteria were: (a) the presence of other tumors in the pancreas, (b) insufficient CT quality, and (c) the presence of other malignancies. Patients who did not undergo NAT were divided into the training and validation sets, which comprised the primary cohort. Patients who underwent NAT formed the internal test set used to assess the robustness of the model.

In the second phase, we retrospectively collected data from 176 patients with PDAC for an external test set at No. 411 hospital between April 2022 and April 2023. The inclusion and exclusion criteria were the same as those previously described (Fig. 1). The details of sample size estimation are shown in Supplement Materials, Supplemental Digital Content 2, http://links.lww.com/JS9/C501.

CT scanning

The CT scanners and scanning parameters for each institution were shown in Supplement Table 1, Supplemental Digital Content 2, http://links.lww.com/JS9/C501. An initial cross-sectional non-enhanced CT scan was performed, followed by a dynamic contrast-enhanced CT scan. Contrast-enhanced CT was performed during the arterial (20–25 s), portal venous (60–70 s), and delayed (110–130 s) phases. The contrast agent (90–95 ml of 355 mgI/ml iopromide [Ultravist 370; Bayer Schering Pharma] was injected at a rate of 5.5 ml/sec using a power injector (Medrad Mark V Plus; Bayer) via the forearm vein, followed by 98 ml of normal saline to flush the tube.

Data acquisition and radiologic image analysis

Original cross-sectional images of the portal phases were used for radiological analysis. Two abdominal radiologists (Y.B. and J.Y.Y) with 25 and 5 years of experience, respectively, assessed images blindly to clinical and pathologic details. In cases of disagreement, a senior radiologist (C.W.S.) was consulted.

Tumors were assessed: (a) CT-reported tumor size from the last preoperative image; (b) location (pancreatic head, body, tail); (c) pancreatic duct cut-off and dilation (> 3 mm); (d) common bile duct cut-off and dilation (> 10 mm); (e) parenthetical atrophy (the anteroposterior diameter of the pancreatic parenchyma (excluding the pancreatic duct) was smaller than 15 mm)[22]; (f) contour abnormality (mass protruding from pancreas contour); (g) cyst presence (pseudo or retention cysts).

For NAT patients, in addition to evaluating the above radiologic features, we also measured the tumor size based on pre-NAT and last preoperative CT scans, according to the RECIST 1.1 guidelines[23]. After NAT, patients were categorized into complete response (CR), partial response (PR), stable disease (SD), and progressive disease (PD) groups, then grouped into treatment-effective (CR and PR) and treatment-ineffective (SD and PD) groups.

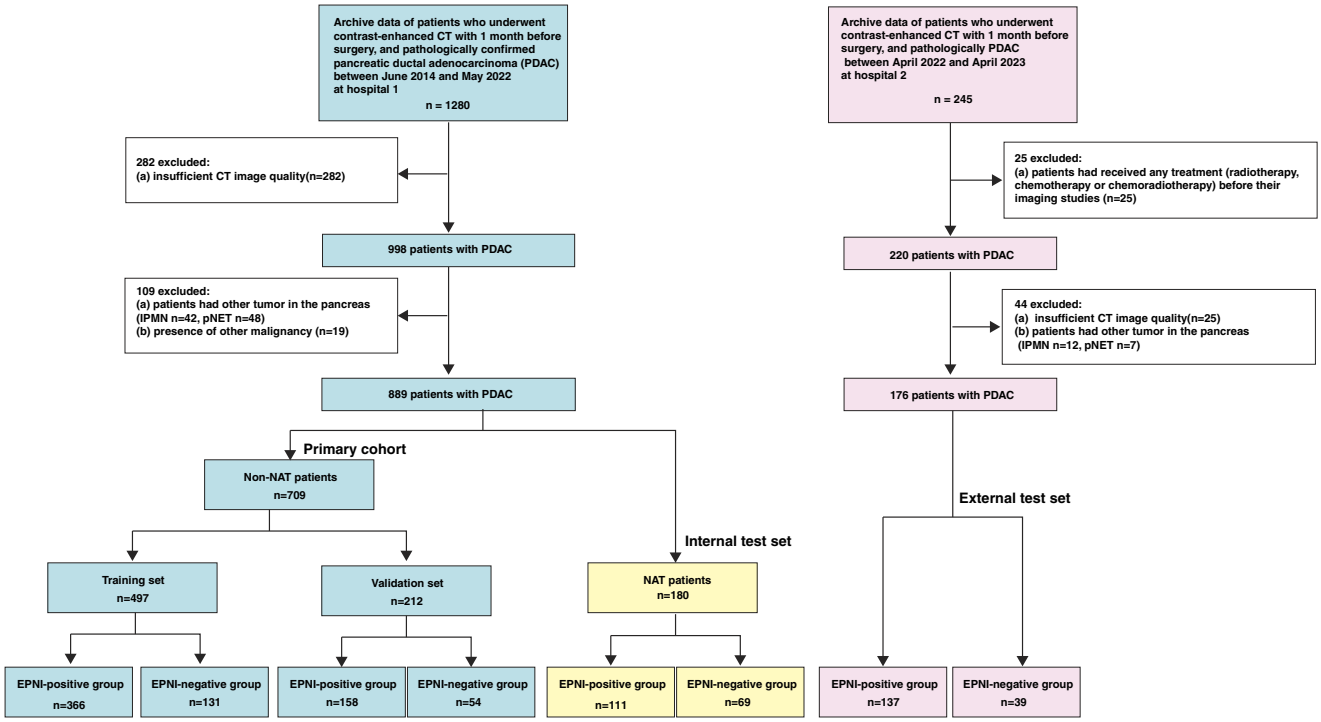

Figure 1. Flow chart visualizing the patient selection process. CT, computed tomography; EPNI, extrapancreatic perineural invasion; IPMN, intraductal papillary mucinous neoplasm; pNET, pancreatic neuroendocrine tumor.

Histopathological analysis

Surgical specimens were subjected to blinded histopathological examination by two pathologists with 15 and 5 years of experience, respectively, who consulted senior pathologists in case of disagreements. EPNI was defined as the presence of viable tumor cells in the perineural space without benign pancreatic tissue surrounding the nerve fibers, including the islets of Langerhans, pancreatic acinar, and benign pancreatic tubules[14,15,24].

Details of other factors that need to be recorded are presented in the Supplementary Materials, Supplemental Digital Content 2, http://links.lww.com/JS9/C501.

EPNI prediction algorithm development and validation

Initially, we located the pancreatic plexus anatomically and reviewed relevant literature. Next, we identified important adjacent blood vessels including the proper hepatic artery (PHA), gastroduodenal artery (GDA), SMV jejunenteric trunk (SMV-JT), abdominal aorta (AA), CHA, CA, PV, SA, SMA, and PIPDA[6,14,25].

We employed the nnUNet (https://github.com/MIC-DKFZ/nnUNet) framework for vessel and tumor segmentation. This tool auto-selects training parameters and models, offering a comprehensive training pipeline for both 2D image and 3D volume segmentation tasks, as depicted in Fig. 2.

Annotation

In this study, CT images from all patients' sets were delineated using ITK-SNAP software (version 3.6.0-RC1; http://www.itksnap.org) by an experienced radiologist 1 with 15 years of pancreatic imaging expertise. The internal test set utilized the last preoperative CT image post-NAT, and the pixel-level annotations of the tumor and vessels were drawn in the portal phase CT image. We opted for the portal venous phase over the arterial phase due to clearer tumor boundaries, aiding segmentation. For inter-observer reliability, radiologist 2 delineated regions of interest (ROIs) for 50 randomly selected patients, while a month later, radiologist 1 reassessed a distinct set of 50 patients to gauge intra-observer reliability. The Dice similarity coefficient (DSC) was used to evaluate the agreement, including inter-observer, intra-observer, and between artificial intelligence (AI) segmentation and the radiologist 1. DSCs was interpreted as follows:less than 0.6 signified poor, 0.6–0.8 moderate, and greater than 0.8 nearly excellent agreement.

Preprocessing

Second, the preprocessed training data were subjected to image normalization and voxel-spacing adjustment. The former involves normalizing the data using the global foreground mean and standard deviation, whereas the latter resamples all training images and masks using third-order spline interpolation.

Network architecture

The nnUNet framework is based on the classic DUnet network in terms of its structure, including network depth, kernel size, and pooling operations. However, it does not incorporate commonly used components such as residual, dense, or inception blocks. In comparison with the classical U-Net framework, padded convolutions were utilized to achieve identical output and input shapes, along with instance normalization.

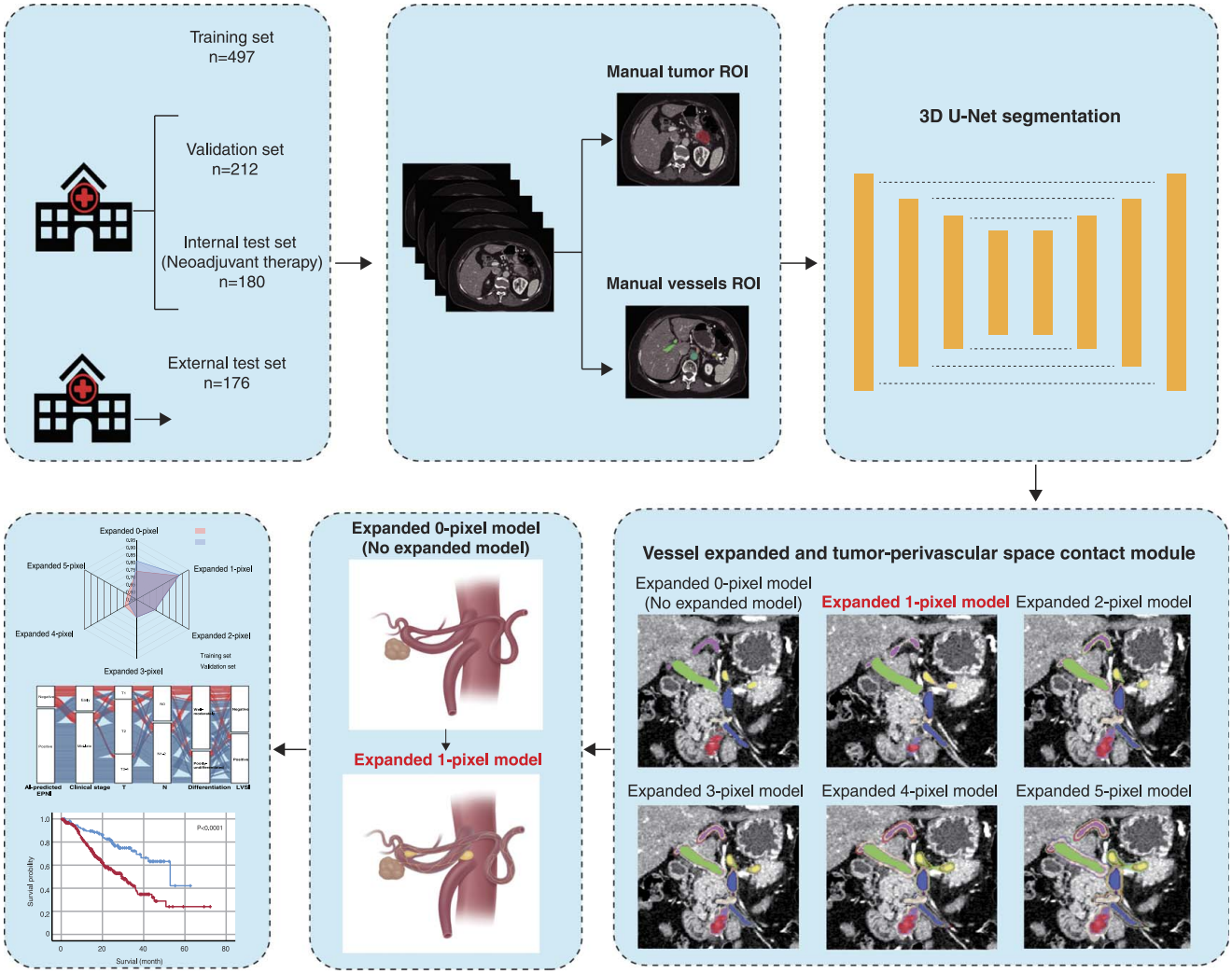

Figure 2. Artificial intelligence (AI) workflow and study flowchart. 3D, three-dimensional; EPNI, extrapancreatic perineural invasion; LVSI, lymph-vascular space invasion; PDAC, pancreatic ductal adenocarcinoma; ROI = region of interest.

Network training

During training, segmentation models underwent five-fold cross-validation and were trained for 1000 epochs using both the cross-entropy and dice loss functions to optimize the model parameters with the Adam optimizer. The initial learning rate was set to 1e-2, and data augmentation techniques such as rotation, left-right flipping, and other transformations were employed to enhance the robustness of the model.

The dropout layer in the network randomly drops some part of our CNN network during training, avoiding to learn redundant representations and reducing reliance on specific neurons.

Expand

To assess the nerve plexus morphology relative to surrounding vessels and tumors, vessel segmentation labels were expanded using Python 3.7 with the skimage package (http://scikit-image.org)[26]. Using a segmentation mask, the scikit-image package expands the label area by 1–5 pixels. We then assessed overlap between the tumor mask and vessel masks pre-expansion and post-expansion.

Classification

The classifier module mainly determines whether the sample is positive or negative EPNI based on whether there is an overlapping volume (contact status) between the blood vessels boundary and the tumor. Specifically, through the above steps, we obtained the segmentation results of tumors and 9 blood vessels boundary. First, we project the segmentation results of tumors and blood vessels boundary into three-dimensional space, and calculate the overlapping volume between the tumor and each blood vessel boundary. Second, the designed algorithm determines whether there is an overlapping volume between each blood vessel boundary and the tumor. If the overlapping volume is greater than 0, this case is classified as EPNI-positive, and the contrary is EPNI-negative.

Table 1

Baseline characteristics of patients with pancreatic ductal adenocarcinoma.

Characteristics	Training set			Validation set			Internal test set			External test set		
	EPNI-negative	EPNI-positive		EPNI-negative	EPNI-positive		EPNI-negative	EPNI-positive		EPNI-negative	EPNI-positive	
	(*n* = 131)	(*n* = 366)	*P*	(*n* = 54)	(*n* = 158)	*P*	(*n* = 69)	(*n* = 111)	*P*	(*n* = 39)	(*n* = 137)	*P*
Clinical characteristics												
Sex, *n* (%)			0.48			0.84			0.86			0.73
M	84 (64.1)	247 (67.5)		36 (66.7)	103 (65.2)1		27 (39.1)	42 (37.8)		22 (56.4)	73 (53.3)	
F	47 (35.9)	119 (32.5)		18 (33.3)	55 (34.8)		42 (60.9)	69 (62.2)		17 (43.6)	64 (46.7)	
Age (year)[a]	63 ± 8	64 ± 10	0.10	63 ± 9	62 ± 10	0.83	61 ± 8	60 ± 10	0.60	63 ± 10	64 ± 9	0.56
BMI (kg/m^2)[a]	22.3 ± 2.5	22.6 ± 2.5	0.38	22.8 ± 3.1	23.3 ± 2.9	0.32	22.7 ± 2.6	23.3 ± 2.8	0.15	23.6 ± 3.9	22.7 ± 2.9	0.12
Surgery, *n* (%)			0.89			0.89			0.06			0.53
Pancreaticoduodenectomy	85 (64.9)	240 (65.6)		36 (66.7)	105 (66.5)		44 (63.8)	55 (49.5)		28 (71.8)	105 (76.6)	
Distal or total pancreatectomy	46 (35.1)	126 (34.4)		18 (33.3)	53 (33.5)		25 (36.2)	56 (50.5)		11 (28.2)	32 (23.4)	
CA 19-9 (U/ml)[b]	121 (34, 614)	203 (45, 1100)	0.14	130 (16, 544)	202 (38, 982)	0.25	113 (40, 614)	252 (29, 810)	0.12	1200 (158,1200)	845 (160, 1200)	0.34
Abdominal pain, *n* (%)			< 0.001			0.03			0.86			0.002
No	77 (58.8)	140 (38.3)		27 (50.0)	53 (33.5)		22 (31.9)	34 (30.6)		25 (64.1)	49 (35.8)	
Yes	54 (41.2)	226 (61.7)		27 (50.0)	105 (66.5)		47 (68.1)	77 (69.4)		14 (35.9)	88 (64.2)	
Pathological characteristics												
T category, *n* (%)			< 0.001			0.01			< 0.001			0.08
T0	0 (0.0)	0 (0.0)		0 (0.0)	0 (0.0)		6 (9.7)	0 (0.0)		0 (0.0)	0 (0.0)	
T1	34 (26.0)	38 (10.4)		13 (24.1)	13 (8.2)		33 (47.8)	22 (19.8)		12 (30.8)	21 (15.3)	
T2	71 (54.2)	215 (58.7)		29 (53.7)	86 (54.5)		26 (37.7)	64 (57.7)		23 (59.0)	93 (67.9)	
T3-4	26 (19.8)	113 (30.9)		12 (2.2)	59 (37.3)		4 (5.8)	25 (22.5)		4 (10.2)	23 (16.8)	
N category, *n* (%)			< 0.001			0.009			< 0.001			0.002
N0	76 (58.0)	109 (29.8)		28 (51.9)	48 (30.4)		45 (65.2)	42 (37.8)		25 (64.1)	48 (35.1)	
N1	43 (32.8)	176 (48.1)		19 (35.1)	65 (41.1)		20 (29.0)	44 (39.6)		12 (30.8)	58 (42.3)	
N2	12 (9.2)	81 (22.1)		7 (13.0)	45 (28.5)		4 (5.8)	25 (22.5)		2 (5.1)	31 (22.6)	
Differentiation grade, *n* (%)			0.05			0.004			0.69			0.05
Well moderately	98 (74.8)	239 (65.3)		43 (79.6)	91 (57.6)		51 (73.9)	85 (76.6)		30 (76.9)	122(89.1)	
Poorly undifferentiated	33 (25.2)	127 (34.7)		11 (20.4)	67 (42.4)		18 (26.1)	26 (23.4)		9 (23.1)	15 (10.9)	
LVSI, *n* (%)			< 0.001			< 0.001			0.02			< 0.001
Negative	87 (66.4)	155 (42.3)		39 (72.2)	62 (39.2)		58 (84.1)	76 (68.5)		31 (79.5)	61 (44.5)	
Positive	44 (33.6)	211 (57.7)		15 (27.8)	96 (60.8)		11 (15.9)	35 (31.5)		8 (20.5)	76 (55.5)	
TRG, *n* (%)			/			/			< 0.001			/
0	/	/		/	/		6 (8.7)	0 (0.0)		/	/	
1	/	/		/	/		13 (18.8)	4 (3.6)		/	/	
2	/	/		/	/		38 (55.1)	73 (65.8)		/	/	
3	/	/		/	/		12 (17.4)	34 (30.6)		/	/	
Clinical stage, *n* (%)			< 0.001			< 0.001			< 0.001			0.001
Early stage	62 (47.3)	71 (19.4)		23 (42.6)	28 (17.7)		42 (60.9)	33 (29.7)		23 (59.0)	42 (30.7)	
Advanced stage	69 (52.7)	295 (80.6)		31 (57.4)	130 (82.3)		27 (39.1)	78 (70.3)		16 (41.0)	95 (69.3)	
CT characteristics												
CT-determined tumor size (cm)[a]	2.9 ± 1.2	2.9 ± 1.2	0.36	2.9 ± 1.2	2.8 ± 1.1	0.30	1.9 ± 1.1	2.7 ± 1.2	< 0.001	2.4 ± 0.8	2.8 ± 0.9	0.022
RECIST1.1, *n* (%)			/			/			0.003			/
CR	/	/		/	/		0 (0.0)	0 (0.0)		/	/	
PR	/	/		/	/		30 (62.3)	22 (77.5)		/	/	
SD	/	/		/	/		10 (2.9)	25 (3.6)		/	/	

PD	/	/		/	/		29 (11.6)	64 (16.2)		/	/	
Location, *n* (%)			0.75			0.98			0.08			0.36
Head	89 (67.9)	243 (66.4)		36 (66.7)	105 (66.5)		47 (68.1)	61 (55.0)		28 (71.8)	108(78.8)	
Neck, body, and tail	42 (32.1)	123 (33.6)		18 (33.3)	53 (33.5)		22 (31.9)	50 (45.0)		11 (28.2)	29 (21.2)	
Pancreatic duct cut-off and dilation, *n* (%)			0.71			0.30			0.18			0.03
No	29 (22.1)	87 (23.8)		15 (27.8)	33 (20.9)		21 (30.4)	24 (21.6)		16 (41.0)	32 (23.4)	
Yes	102 (77.9)	279 (76.2)		39 (72.2)	125 (79.1)		48 (69.6)	87 (78.4)		23 (59.0)	105(76.6)	
Common bile duct cut-off and dilation, *n* (%)			0.32			0.44			0.99			0.70
No	69 (52.7)	211 (57.7)		34 (63.0)	90 (34.7)		54 (78.3)	87 (78.4)		21 (53.8)	69 (50.4)	
Yes	62 (47.3)	155 (42.3)		20 (27.0)	68 (34.7)		15 (21.7)	24 (21.6)		18 (46.2)	68 (49.6)	
Parenchymal atrophy, *n* (%)			0.92			0.21			0.04			< 0.001
No	53 (40.5)	150 (41.0)		25 (46.3)	58 (34.7)		52 (75.4)	67 (60.4)		15 (38.5)	20 (14.6)	
Yes	78 (59.5)	216 (59.0)		29 (53.7)	100 (34.7)		17 (24.6)	44 (39.6)		24 (61.5)	117(85.4)	
Contour abnormality, *n* (%)			0.19			0.78			0.07			0.12
No	52 (39.7)	122 (33.3)		21 (38.9)	58 (36.7)		22 (31.9)	22 (19.8)		13 (33.3)	29 (21.2)	
Yes	79 (60.3)	244 (66.7)		33 (61.1)	100 (63.3)		47 (68.1)	89 (80.2)		26 (66.7)	108 (78.8)	
Cyst, *n* (%)			0.68			0.91			0.43			0.14
No	121 (92.4)	342 (93.4)		50 (92.6)	147 (93.0)		58 (84.1)	88 (79.3)		34 (87.2)	129 (94.2)	
Yes	10 (7.6)	24 (6.6)		4 (7.4)	11 (7.0)		11 (15.9)	23 (20.7)		5 (12.8)	8 (5.8)	

Except where indicated, data are numbers of patients, with percentages in parentheses.

CR, complete response; CT, computed tomography; EPNI, extrapancreatic perineural invasion; F, female; IQR, interquartile range; LVSI, lymph-vascular space invasion; M, male; NAT, neoadjuvant therapy, PD, progressive disease; PR, partial response; RECIST, response evaluation criteria in solid tumors; SD, stable disease; TRG, tumor regression grade.

[a]Data are means ± SDs.

[b]Data are median (IQR).

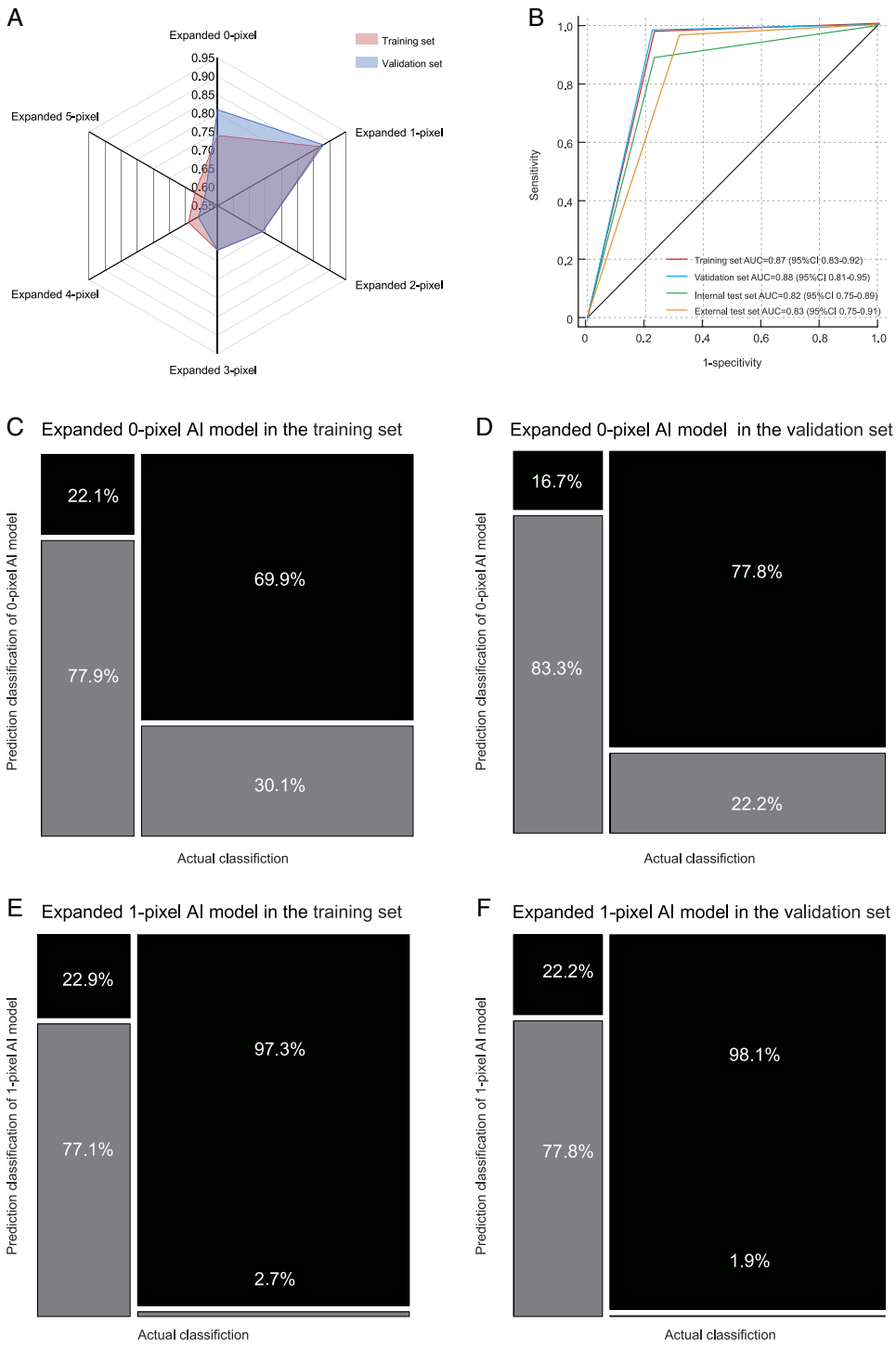

Figure 3. The performance and classification of artificial intelligence (AI) model. (A) Radar map of receiver operating characteristic curves of the six intelligence (AI) models in the training and validation sets. (B) Receiver operating characteristic curves of the AI model with a 1-pixel expansion in the training, validation, internal test, and external test sets. (C) Mosaic plot of the AI model with a 0-pixel expansion in the training set. (D) Mosaic plot of the AI model with a 0-pixel expansion in the validation set. (E) Mosaic plot of the AI model with a 1-pixel expansion in the training set. (F) Mosaic plot of the AI model with a 1-pixel expansion in the validation set.

The pathological correlation with radiology

The details are illustrated in Supplementary Figure 1, Supplemental Digital Content 2, http://links.lww.com/JS9/C501.

Statistical analyses

For group comparisons, *t*-test (normal distribution), rank sum test (skewed distribution), and χ^2test (categorical variables) were used. ROC curves were plotted to evaluate the AI model performance. Evaluation metrics, including area under the curve (AUC), accuracy, sensitivity, and specificity, with a 95% CI were computed. Overall survival (OS) times spanned from surgery to death or last follow-up, conducted on 20 February 2023. Death was considered an event, and patients lost to follow-up were censored. Kaplan–Meier estimates were used to plot survival curves, whereas the log-rank test was used to assess differences between the curves. Univariate and multivariate Cox regression analyses were conducted to examine the relationship between the AI-predicted EPNI and OS. Statistical *P* value was set at *P* less than 0.05. All analyses were performed using the R software (version 3.3.3; R Foundation for Statistical Computing; https://www.r-project.org/).

System and environment

The specific system of the model, as well as detailed configurations of hardware and optimizer, are presented in the Supplementary Materials, Supplemental Digital Content 2, http://links.lww.com/JS9/C501. The prediction AI model, inference code, and illustrative examples of the CT images, tumors, and vessel masks are publicly available on GitHub (https://github.com/CHANGHAI-AILab/segmentation_expand_labels).

Result

Study design and patient characteristics

The study design is described in Fig. 2. The training set included 497 patients from June 2014 to October 2019, whereas the independent validation set had 212 patients from October 2019 to May 2022. The internal and external test sets comprised 180 and 176 patients, respectively.

Significant differences existed in N categories, LVSI, and clinical stage between EPNI-positive and EPNI-negative groups across all sets ($P < 0.05$), as well as in T categories within the training, validation, and internal test sets ($P < 0.05$). Patient characteristics were detailed in Table 1.

Manual delineation reproducibility and automated segmentation accuracy

We assessed the inter-observer and intra-observer reproducibility of vessel and tumor segmentation, and compared the accuracy of AI model segmentation(Supplementary Materials, Supplemental Digital Content 2, http://links.lww.com/JS9/C501).

EPNI prediction accuracy

We expanded the vessel boundary by 1–5 pixels to create five perivascular spaces and developed six models with 0–5 pixels. EPNI was determined by vessel boundary contact with the tumor: negative if no contact, positive if contact occurred. The performance of the six models was presented in Supplementary Table 2, Supplemental Digital Content 2, http://links.lww.com/JS9/C501 and Fig. 3A. Our analysis revealed that the model with a 1-pixel expansion had the highest AUC in the validation set and was selected as the final diagnostic model. The AUC of the 1-pixel expansion model was 0.87 (95% CI: 0.83–0.92), 0.88 (95% CI: 0.81–0.95), 0.82 (95% CI: 0.75–0.89), and 0.83 (95% CI: 0.75–0.91) in the training, validation, internal test, and external test sets, respectively (Fig. 3B and Table 2).

In addition, we compared the accurate identification of the 0-pixel expansion model with the 1-pixel expansion model in the training and validation sets (Fig. 3C-F). Two illustrative cases diagnosed using this model were shown in Fig. 4.

Association between AI-predicted EPNI and OS

In the training, validation, and internal test sets, 26, 16, and 24 patients, respectively, were unreachable after surgery. In addition, we excluded survival data from the external test set because they were obtained from patients within a year post-surgery. In the training set, the median survival time was 52.9 months (95% CI: 35.3–70.5 months) and 29.5 months (95% CI: 25.0–34.0 months) in the EPNI-negative and EPNI-positive groups, respectively. In the validation set, the median survival time was 37.7 months (95% CI: 28.4–46.9 months) and 24.8 months (95% CI: 18.7–30.9 months) in the EPNI-negative and EPNI-positive groups, respectively. In the internal test set, the median follow-up duration was 69.8 months (95% CI: 38.0–101.6 months) and 40.3 months (95% CI: 28.9–51.7 months) in EPNI-negative and EPNI-positive groups, respectively.

The log-rank test indicated longer survival in the predicted EPNI-negative group compared to the EPNI-positive group (training set, $P < 0.001$; validation set, $P = 0.049$; internal test set, $P = 0.003$) (Fig. 5A–C). In univariate analysis, positive AI-

Table 2

The performance of expanded 1-pixel AI model in four sets.

Performance	Training set	Validation set	Internal test set	External test set
AUC[a]	0.87 (0.83, 0.92)	0.88 (0.81, 0.95)	0.82 (0.75, 0.89)	0.83 (0.75, 0.91)
Sensitivity	97.3 (356/366)	98.1 (155/158)	96.4 (107/111)	89.1 (122/137)
Specificity	77.1 (101/131)	77.8 (42/54)	68.1 (47/69)	76.9 (30/39)
Accuracy	92.0 (457/497)	92.9 (197/212)	85.6 (154/180)	86.4 (152/176)
PPV	92.2(356/386)	92.8 (155/167)	82.9 (107/129)	93.1 (122/131)
NPV	91.0 (101/111)	93.3 (42/45)	92.2 (47/51)	66.7 (30/45)

Except where indicated, data are percentages, with numbers of patients in parentheses. Performance is presented as AUC, sensitivity, and specificity values according to the optimal selected cut-off.
AI, artificial intelligence; AUC, area under the receiver operating characteristic curve; NPV, negative predictive value; PPV, positive predictive value.
[a]Data are AUCs, with 95% CIs in parentheses.

predicted EPNI was correlated with poorer survival [hazard ratio (HR), 2.21; 95% CI: 1.59–3.07; $P < 0.001$] within the primary cohort. Multivariate Cox regression confirmed AI-predicted EPNI was an independent preoperative predictor of worse OS (HR, 1.51; 95% CI: 1.05–2.15; $P = 0.02$) (Table 3). Similar results were obtained for the internal test set (Supplementary Table 3, Supplemental Digital Content 2, http://links.lww.com/JS9/C501).

Primary subgroup analysis

We explored the feasibility of applying AI-predicted EPNI to various patient subgroups across various pathological strata, including the T category, N category, LVSI, differentiation, and clinical stage in the primary cohort. The log-rank test revealed a longer survival duration in the predicted EPNI-negative group than in the predicted EPNI-positive group (T1, $P = 0.041$; T2, $P = 0.003$). Similarly, significant differences in OS were observed between the EPNI-negative and EPNI-positive groups when stratified by N category (N0, $P = 0.003$; N1-2, $P = 0.014$), LVSI (positive, $P = 0.004$; negative, $P = 0.004$), well-moderately differentiated tumors ($P < 0.001$), and clinical stage (early stage, $P = 0.004$; advanced stage, $P = 0.036$) in the primary cohort. The results of the pathological subgroups were shown in Fig. 5D–N. The Sankey diagram presented the patient distribution among the AI-predicted EPNI-negative or EPNI-positive groups, clinical stage, T category, N category, LVSI, and differentiation (Fig. 5O).

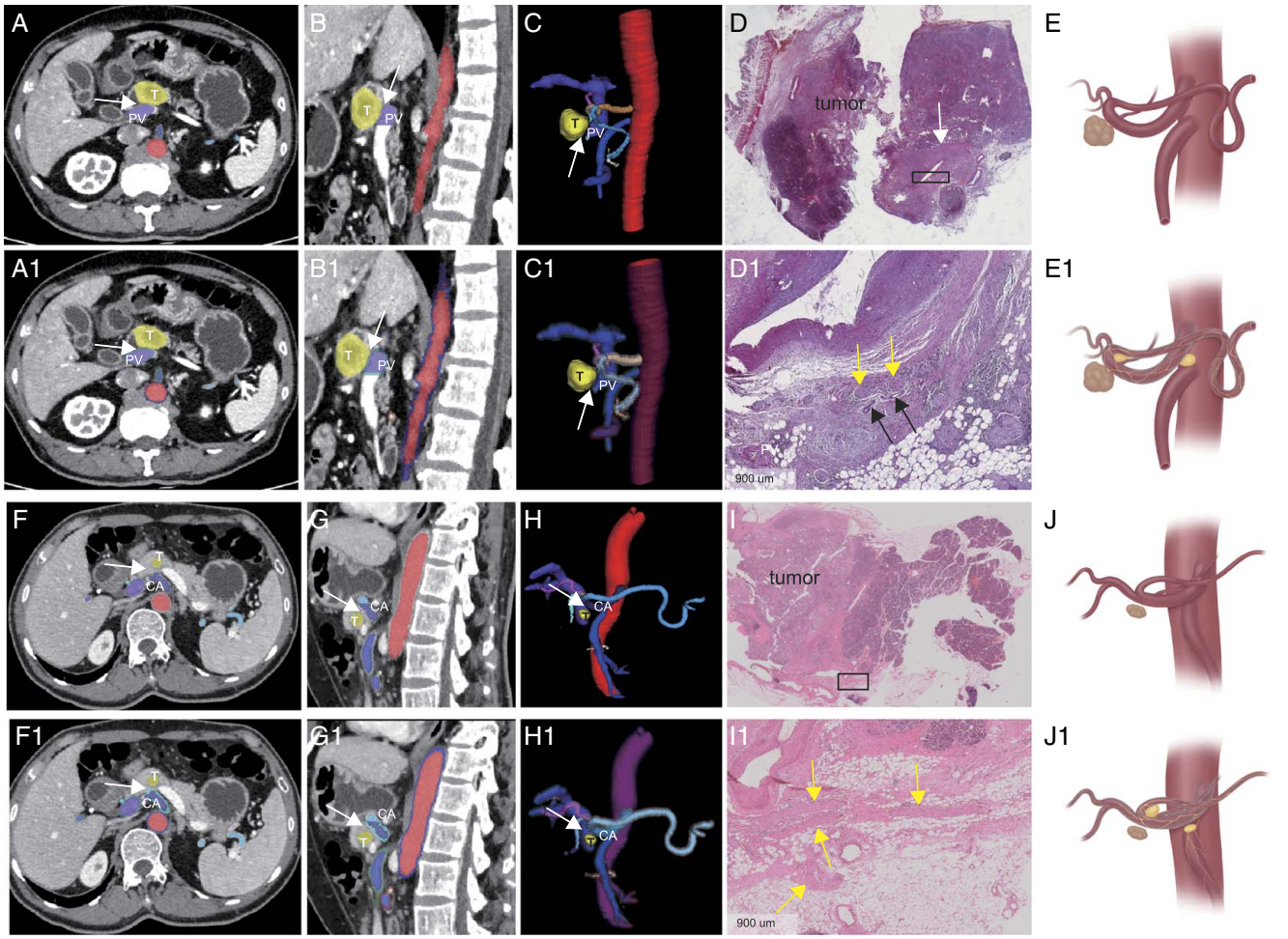

Figure 4. Comparison of patients with extrapancreatic perineural invasion (EPNI) positive and negative. (A–E1) Patient 1: a 71-year-old man with pancreatic ductal adenocarcinoma (PDAC) in the EPNI-positive group. The tumor and portal vein (PV) are not in contact in the 0-pixel artificial intelligence (AI) model, but they are in contact in the 1-pixel AI model. (A) and (A1), (B) and (B1), and (C) and (C1) are the cross-sectional, sagittal PV phase computed tomography (CT) images and three-dimensional (3D) images corresponding to 0-pixel and 1-pixel AI models, respectively. (D) Hematoxylin-eosin stain shows that the peritumoral extrapancreatic nerve cells are positive (magnification, 1 ×), (D1) The black box in Figure D highlights the area where the peritumoral extrapancreatic nerve cells are positive (yellow arrows: nerve cells, black arrows: tumors) (hematoxylin-eosin staining; magnification, 20 ×). (E) The 3D diagram shows the tumor and vessels are not in contact. (E1) The 3D diagram shows the vascular boundary is expanded by 1 pixel; the nerve plexus is in contact with the tumor within the perivascular space. (F–J1) Patient 2: a 59-year-old man with PDAC in the EPNI-negative group. The tumor and celiac trunk (CA) are not in contact in the 0-pixel and 1-pixel AI models. (F) and (F1), (G) and (G1), and (H) and (H1) are the cross-sectional, sagittal PV phase CT images and three-dimensional (3D) images corresponding to 0-pixel and 1-pixel AI models, respectively, (I) Hematoxylin-eosin stain shows that the peritumoral extrapancreatic nerve cells are negative (magnification, 1 ×), (I1) The black box in Figure I highlights the area where the peritumoral extrapancreatic nerve cells are negative (yellow arrows: nerve cells) (hematoxylin-eosin staining; magnification, 20 ×). (J) The 3D diagram shows the tumor and vessels are not in contact. (J1) The 3D diagram shows that the vascular boundary has been expanded by 1 pixel, but the nerve plexus is still not in contact with the tumor within the perivascular space.

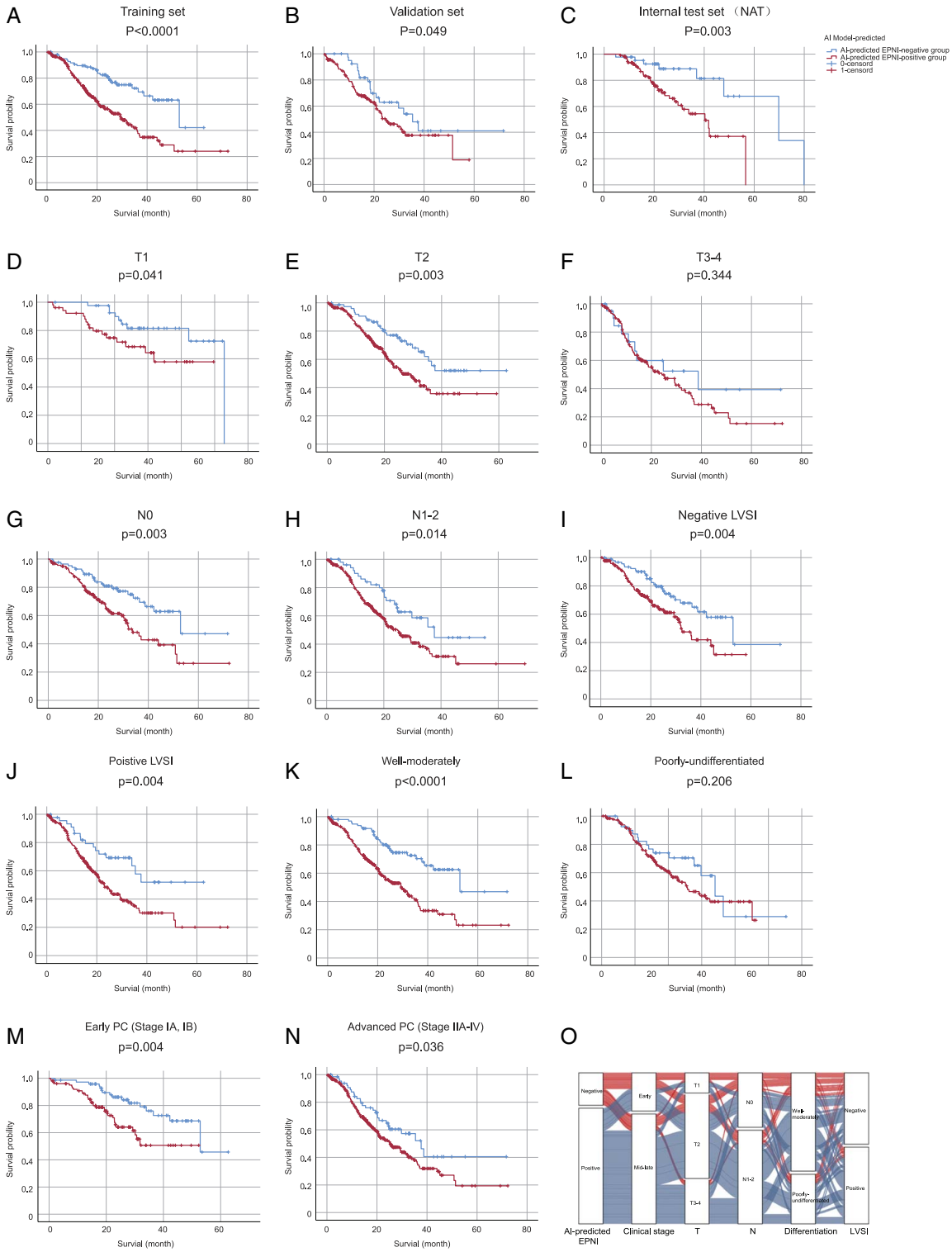

Figure 5. Classification and survival analysis of the 1-pixel artificial intelligence (AI) model. The Kaplan–Meier survival curves shows significantly longer survival for patients in the AI-predicted extrapancreatic perineural invasion (EPNI)-negative group than those in the AI-predicted EPNI-positive in the training, validation, and the internal test sets. (A) Training set, (B) validation set, (C) The internal test set. The Kaplan–Meier survival curves show significantly longer survival for patients in the AI-predicted EPNI-negative group than those in the AI-predicted EPNI-positive group in T1, T2, N0, N1-2, positive and negative lymphovascular space invasion (LVSI) status, well differentiation, and early and advanced clinical stages. (D–F) T1, 2, and 3-4 categories; (G–H) N0 and N1-2 categories; (I, J) positive and negative LVSI status; (K, L) well and poorly differentiated; (M, N) early and advanced clinical stages. (O) The Sankey diagram shows the correspondence relationships of AI-predicted EPNI subgroups among all patients with clinical stage, T categories, N categories, LVSI, and differentiation in the primary cohort.

Table 3

Clinical and pathologic characteristics and AI model–predicted EPNI associated with worse overall survival in primary cohort.

	Univariable analysis		Multivariable analysis	
Variable	**Hazard ratio**	***P***	**Hazard ratio**	***P***
Sex				
F	1.0			
M	0.89 (0.69, 1.14)	0.35		
Age (per year)	1.02 (1.00, 1.03)	0.01	1.02 (1.01, 1.04)	0.004
Operation				
Pancreaticoduodenectomy	1.0			
Distal or total pancreatectomy	0.98 (0.76, 1.26)	0.87		
Abdomen pain				
No	1.0		1.0	
Yes	1.39 (1.09, 1.78)	0.01	1.29 (1.00, 1.67)	0.05
BMI (per kg/m^2)	0.98 (0.93, 1.02)	0.34		
CA199				
≤37 U/ml	1.0		1.0	
>37 U/ml	1.35 (1.00, 1.82)	0.046	1.18 (0.88, 1.60)	0.27
T category				
1	1.0		1.0	
2	1.91 (1.26, 2.93)	0.003	1.50 (0.96, 2.36)	0.08
3–4	2.87 (1.85, 4.45)	<0.001	2.18 (1.30, 3.66)	0.003
N category				
0	1.0		1.0	
1	1.52 (1.15, 2.01)	0.004	1.30 (0.84, 2.02)	0.24
2	2.40 (1.73, 3.33)	<0.001	1.91 (1.17, 3.09)	0.009
Clinical stage				
Early stage	1.0		1.0	
Advanced stage	2.22 (1.63, 3.03)	<0.001	1.09 (0.63,1.89)	0.76
Differentiation				
Well moderately	1.0			
Poorly undifferentiated	1.19 (0.92, 1.53)	0.19		
LVSI				
Negative	1.0		1.0	
Positive	1.61 (1.26, 2.06)	<0.001	1.25 (0.96, 1.62)	0.10
Location				
Head	1.0			
Neck, body and tail	1.04 (0.81, 1.33)	0.77		
Size (per cm)	1.01 (1.00, 1.02)	0.14		
Pancreatic duct cut-off and dilation				
No	1.0		1.0	
Yes	1.61 (1.18, 2.20)	0.003	1.64 (1.20, 2.26)	0.002
Common bile duct cut-off and dilation				
No	1.0			
Yes	0.91 (0.71, 1.17)	0.46		
Profile				
No	1.0			
Yes	1.08 (0.84, 1.38)	0.57		
Cystic				
No	1.0			
Yes	1.09 (0.69, 1.73)	0.70		
Parenchyma				
No	1.0			
Yes	1.19 (0.93, 1.52)	0.18		
AI-predicted EPNI				
Negative	1.0		1.0	
Positive	2.21 (1.59, 3.07)	<0.001	1.51 (1.05, 2.15)	0.02

Data in parentheses are 95% CIs. There were 709 patients and 267 deaths.

AI, artificial intelligence; EPNI, extrapancreatic perineural invasion; F, female; LVSI, lymph-vascular space invasion; M, male.

NAT subgroup analysis

A total of 180 patients underwent NAT, including 69 EPNI-negative (38.3%) and 111 EPNI-positive (61.7%) patients. OS was not different between TRG response and between RECIST1.1 classification ($P = 0.291$, $P = 0.239$) (Fig. 6A and B).

Furthermore, we assessed the AI model combined TRG (Supplementary Table 4, Supplemental Digital Content 2, http://links.lww.com/JS9/C501) and RECIST1.1 (Supplementary Table 5, Supplemental Digital Content 2, http://links.lww.com/JS9/C501). Significant differences were observed in the combination of the AI model with TRG ($P = 0.026$) and the AI model and RECIST1.1 ($P = 0.016$) (Fig. 6C and D).

Discussion

In this study, we redefined the perivascular space as a key area that encompasses the peripheral pancreatic nerve plexus, acting as a vital site for the manifestation of EPNI. Building on this innovative perspective, we developed and validated a deep-learning algorithm tailored for automated segmentation of tumors and adjacent vessels. We delineated the perivascular space by extending the vascular boundaries, allowing us to automate the assessment of tumor contact with the perivascular space, effectively simulating the encroachment of the neoplasm into the pancreatic nerve plexus, and significantly enhancing the interpretability and understanding of our model's analytical processes. The AI model demonstrated exceptional efficacy across various cohorts with AUC values of 0.87, 0.88, 0.82, and 0.83 in the training, validation, internal test, and external test sets, respectively. Furthermore, the EPNI identified by the AI was an independent prognosis factor and correlated with poorer survival outcomes in the primary cohort (HR, 1.51; $P = 0.02$), and the internal test set (HR, 2.59; $P = 0.04$). Notably, among patients with early-stage disease (stage IA and IB), those identified as EPNI-positive by AI exhibited significantly poorer survival than the EPNI-negative group ($P = 0.004$). Moreover, we found that the integration of AI-identified EPNI with RECIST 1.1 criteria could predict the treatment efficacy in the NAT set more precisely. Therefore, AI-identified EPNI may be a potential indicator for evaluating treatment efficacy in NAT.

Previous conventional studies[14,15] have relied on the direct observation of microstructures. However, these traditional imaging techniques present several challenges. First, the studies included small patient populations, compromising the representativeness and reliability of their findings. Second, the subjective nature of this indicator is affected by the technical expertise of the radiologists, leading to potential issues with clinical reproducibility. Additionally, these imaging characteristics were observed only in a fraction of EPNI-positive patients, highlighting low sensitivity. The challenge lies in distinguishing signs from vascular fibrosis, lymphatic inflammation, or imaging artifacts, reducing specificity. Finally, the diagnostic efficacy of this indicator was moderate, with previous reports suggesting a value of 0.78. Some studies suggest that the proximity of the tumor to the neuroanatomy is crucial. Guo *et al.*[24] used the minimum distance between the tumor boundary and adventitia of the SMA and CA as quantitative indicators of PNI, yielding relatively high sensitivity (74.63%) and specificity (84.31%). However, the distance index in the study was relatively objective, requiring manual measurement, and only evaluated two vessels: CA and SMA.

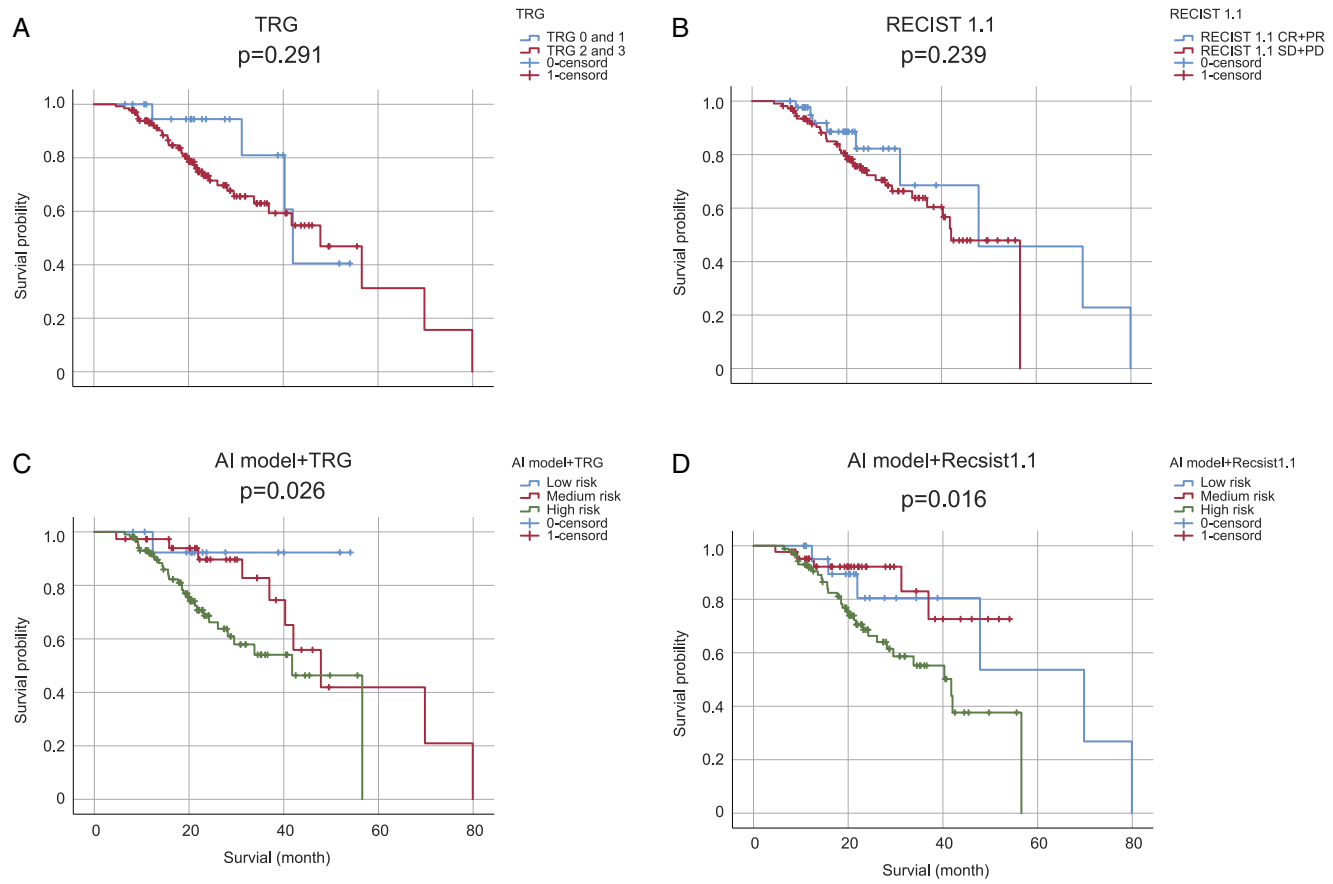

Figure 6. Subgroup survival analysis in the internal test set. The Kaplan–Meier survival curves show significantly longer survival for patients in the artificial intelligence (AI)-predicted extrapancreatic perineural invasion (EPNI)-negative group than those in the AI-predicted EPNI-positive group in the 1-pixel AI model combined with TRG and the 1-pixel AI model combined with RECIST 1.1. (A) tumor regression grade (TRG) 0 + 1 (well-response) vs. TRG 2 + 3 (poor-response), (B) RECIST 1.1 CR + PR (treatment-effective) vs. RECIST 1.1 SD + PD (treatment-ineffective), (C) The 1-pixel AI model combined with TRG, (D) The 1-pixel AI model combined with RECIST 1.1.

However, as research advanced, it became apparent[16,17] that PNI is driven by reciprocal interactions between cancer cells and the nerve microenvironment, including nerve-supporting, inflammatory, and immune cells. This dynamic process involves nerve growth and tumor progression, culminating in the encroachment of the tumor into the nerve plexus. However, the direct visualization of the peripancreatic nerve plexus via imaging remains challenging. Given the proximity of vessels to the neural plexus, we hypothesized that the perivascular space was a crucial area where the neural plexus walks, grows, and where EPNI occurs. To capture the perivascular space, we leveraged deep-learning methods for vessel segmentation and expanded the vascular boundaries by 1–5 pixels to accurately delineate the perivascular space, enabling the quantification of tumor contact with this zone. Our findings indicated that a 1-pixel expansion yields optimal diagnostic performance, with an AUC of 0.87 and 0.88 in the training and validation sets, respectively. Moreover, when no pixels were expanded, the model missed 132 patients with positive EPNI in the primary cohort, lowering the AUC to 0.74 in the training set, 0.81 in the validation set, and underscoring the importance of the perivascular space in precise EPNI identification.

PNI is recognized as an independent prognostic risk factor in various malignancies, closely linked to lymph nodes and distant metastasis[27,28]. Our findings showed that patients AI-predicted EPNI-negative patients exhibited significantly longer survival than EPNI-positive counterparts (training set, $P < 0.001$; validation set, $P = 0.049$; internal test set, $P = 0.003$). Additionally, AI-predicted EPNI-positive emerged as an independent preoperative predictor of worse OS (HR, 1.51; 95% CI: 1.05–2.15; $P = 0.02$), with similar results observed in NAT patients with PDAC (HR, 2.59; 95% CI: 1.06–6.30; $P = 0.04$). Subsequent subgroup survival analysis revealed that the AI-predicted EPNI could stratify survival outcomes within identical T or N stages. Other studies[29] also proposed that PNI independently predicts disease-free survival in patients with PDAC less than or equal to 20 mm and those with R0/N0 status, emphasizing its critical role as an early diagnostic marker. Notably, among patients with early-stage disease (stage IA, IB), those identified as EPNI-positive using AI exhibited significantly poorer survival than the EPNI-negative group ($P = 0.004$). Consequently, our model offers clinicians a tool for more refined prognostic stratification, complementing TNM staging and facilitating the identification of patients at earlier stages. Although surgical resection remains the primary treatment for early-stage pancreatic cancer, the presence of EPNI suggests that neoadjuvant therapy should be considered because of its association with adverse prognoses.

While RECIST 1.1 response is the standard for assessing treatment response in a variety of clinical contexts[30,31], its limitations are increasingly recognized, particularly its inability to detect early metabolic changes within tumors that precede size reduction after cytotoxic therapies[32]. This gap highlights the need for more nuanced approaches to evaluate the efficacy of NAT and preoperatively stratify patient prognosis. Our study did not find a significant correlation between the RECIST 1.1 responses and OS. Instead, we identified AI-predicted EPNI as a strong prognostic factor for OS in NAT patients (HR, 3.51; 95% CI: 1.46–8.45; $P = 0.005$). This finding is consistent with that of Cha *et al.*[33], who reported that the PNI is a determinant of early recurrence in pancreatic cancer post-NAT. To bolster the reliability of our findings, we integrated RECIST 1.1 responses with AI-predicted EPNI, creating a novel risk stratification system that significantly distinguished OS across different risk categories (low-risk vs. high-risk: median OS 69.8 vs. 41.8 months, $P = 0.016$). Our analysis also revealed that TRG was not a significant prognostic marker for patients with NAT, likely because of the high proportion of patients with TRG 2 and 3 in the internal test set (87.2%, 157/180). In addition, we combined TRG classification with AI-predicted EPNI to propose another risk stratification method, which discerned significant OS differences among risk groups (intermediate risk vs. high risk: median OS 47.8 vs. 41.8 months, $P = 0.026$). Thus, our AI model was able to complement information on tumor biology and treatment response. The model combined with RECIST1.1 criteria can refine the preoperative efficacy evaluation and prognosis for NAT patients, aiding in the adjustment of the NAT scheme and informing surgical timing. Postoperatively, the integration of the model with TRG classification can sharpen prognosis predictions and guide adjuvant therapy choices and clinical decision-making.

The opacity of deep-learning models in terms of interpretability has been a barrier to their widespread adoption in healthcare[34,35]. Therefore, recent research initiatives have concentrated on elucidating and interpreting the decision-making processes inherent to these models. While prior studies have employed heat maps as a means of visualizing model decisions, these tools provide limited insight and fail to deliver a deep understanding of the underlying decision-making[36,37]. Our study diverges from conventional deep-learning architectures by utilizing the perivascular space to simulate the dynamic spatial relationship between nerves and cancerous cells. This novel methodology not only augmented the interpretability and comprehension of our model's decision-making but also highlighted the importance of integrating biological principles into deep-learning frameworks to refine clinical decision-making. Moreover, our model autonomously segmented tumors and vessels with excellent precision, achieving mean DSCs of 0.86 and 0.81 for tumors and vessels, respectively, in the validation set and outperforming many existing studies[38–41]. To the best of our knowledge, this is one of the most comprehensive and accurate pancreatic vessel segmentations to date[38]. The automated nature of this segmentation demonstrated remarkable reproducibility, eliminating the variability and challenges associated with manual contouring as well as the need for time-consuming manual corrections typically required in clinical practice. Additionally, the compatibility of the model with various imaging modalities, parameters, and slice thicknesses suggests its potential for widespread adoption across different institutions and platforms.

This study had several limitations that warrant consideration. First, although the multi-institutional design strengthens the robustness of our deep-learning application, an unavoidable bias persists in the distribution of patient populations across the centers. While our incorporation of internal and external test sets aimed to mitigate this bias, future research should endeavor to encompass a more heterogeneous patient cohort to overcome this bias. Second, the mean DSCs for the segmentation of PDAC tumors and vessels stood at 0.86 and 0.81, respectively, indicating excellent agreement with manual segmentation and outperforming the mean values reported in the current literature. However, the AUC of expanded 1-pixel AI model were less than 90%. Nonetheless, the precision of the model in differentiating between tumors and vasculature requires enhancement. Future investigations should focus on improving the segmentation accuracy by potentially increasing the resolution of the input images, integrating a multiphase manual delineation process for the vasculature, and expanding the training dataset to refine the model's segmentation abilities. Third, the specificity of our model was not ideal, which can be attributed to the scarcity of negative samples and inaccuracies in tumor segmentation, resulting in an increased rate of false positives. In response, we intend to broaden the collection of negative samples for validation and fine-tune the tumor segmentation approach. Finally, although this study did not determine the prognostic value of RECIST1.1, and TRG in the NAT population, we found that AI-predicted EPNI can supplement these indicators to assess the treatment response of NAT, even in patients who cannot undergo surgical resection. To reinforce these findings, we will collect more internal and external cases to establish a more representative sample that will improve our model's stratification effect in the NAT population and allow for further validation of its clinical utility and reliability.

In conclusion, we developed a novel preoperative CT-based AI model for the diagnosis of EPNI in pancreatic cancer. The model could independently predict the prognosis of patients with pancreatic cancer and achieve more accurate prognosis stratification. Notably, the model also exhibited exceptional prognostic stratification in early pancreatic cancer, providing valuable insights for early clinical decision-making. In addition, the model combined with the RECIST1.1 criteria and TRG could refine treatment efficacy evaluation and prognosis for patients with NAT, guide adjuvant therapy choices, and clinical decision-making.

Ethical approval

The study was approved by the Institutional Ethics Review Board of the Changhai hospital and no.411 hospital and conducted in accordance with the Declaration of Helsinki. the reference number is CHEC-Y2020-011.

Consent

The requirement for informed consent was waived by the institutional review board because of the retrospective nature of the study and because all procedures were performed as part of routine care.

Source of funding

This work was supported in part by the National Science Foundation for Scientists of China (81871352, 82171915, 82171930, 82271972 and 82371955), The Natural Science Foundation of Shanghai Science and Technology Innovation Action Plan (21ZR1478500, 21Y11910300), and Clinical Research Plan of SHDC (SHDC2022CRD028).

Author contribution

Study concept or design: J.Y., C.C.. Data collection: J.Y., X.F., J.L., and M.Z. Formal analysis: J.Y., C.C., X.F., and N.L. Investigation: J.Y., X.Y., J.L., and Y.H. Methodology: J.Y., C.C., L.W., and J.L. Project administration: C.S., Y.B. Writing—original draft: J.Y. Writing—review and editing: J.Y., C.C., M.L., C.S., and Y.B.

Conflicts of interest disclosure

The author declares no conflict of interest.

Research registration unique identifying number (UIN)

This study was registered at ClinicalTrials.gov (trail number: ChiCTR2000038576)

Guarantor

Chengwei Shao and Yun Bian had full access to all the data and verified the underlying data. All authors were involved in reviewing the manuscript and approved the final manuscript for submission.

Data availability statement

The prediction AI model, inference code, and illustrative examples of the CT images, tumors, and vessel masks are publicly available on GitHub (https://github.com/CHANGHAIAILab/segmentation_expand_labels). Data generated or analyzed during the study are available from the corresponding author by request. The original data are not publicly available, but are available from the corresponding author upon reasonable request.

Provenance and peer review

My paper was not invited.

Presentation

None.

References

[1] Rahib L, Smith BD, Aizenberg R, *et al*. Projecting cancer incidence and deaths to 2030: the unexpected burden of thyroid, liver, and pancreas cancers in the United States. Cancer Res 2014;74:2913–21.

[2] Groot VP, Rezaee N, Wu W, *et al*. Patterns, timing, and predictors of recurrence following pancreatectomy for pancreatic ductal adenocarcinoma. Ann Surg 2018;267:936–45.

[3] Schorn S, Demir IE, Haller B, *et al*. The influence of neural invasion on survival and tumor recurrence in pancreatic ductal adenocarcinoma—a systematic review and meta-analysis. Surg Oncol 2017;26:105–15.

[4] Kayahara M, Nakagawara H, Kitagawa H, *et al*. The nature of neural invasion by pancreatic cancer. Pancreas 2007;35:218–23.

[5] Takahashi T, Ishikura H, Motohara T, *et al*. Perineural invasion by ductal adenocarcinoma of the pancreas. J Surg Oncol 1997;65:164–70.

[6] Makino I, Kitagawa H, Ohta T, *et al*. Nerve plexus invasion in pancreatic cancer: spread patterns on histopathologic and embryological analyses. Pancreas 2008;37:358–65.

[7] Mochizuki K, Gabata T, Kozaka K, *et al*. MDCT findings of extrapancreatic nerve plexus invasion by pancreas head carcinoma: correlation with en bloc pathological specimens and diagnostic accuracy. Eur Radiol 2010;20:1757–67.

[8] Patel BN, Giacomini C, Jeffrey RB, *et al*. Three-dimensional volume-rendered multidetector CT imaging of the posterior inferior pancreaticoduodenal artery: its anatomy and role in diagnosing extrapancreatic perineural invasion. Cancer Imaging 2013;13:580–90.

[9] Nagakawa T, Nagamori M, Futakami F, *et al*. Results of extensive surgery for pancreatic carcinoma. Cancer 1996;77:640–5.

[10] Pedrazzoli S, DiCarlo V, Dionigi R, *et al*. Standard versus extended lymphadenectomy associated with pancreatoduodenectomy in the surgical treatment of adenocarcinoma of the head of the pancreas: a multicenter, prospective, randomized study. Lymphadenectomy Study Group. Ann Surg 1998;228:508–17.

[11] Yang YM, Wan YL, Tian XD, *et al*. Outcome of pancreaticoduodenectomy with extended retroperitoneal lymphadenectomy for adenocarcinoma of the head of the pancreas. Chin Med J (Engl) 2005;118:1863–9.

[12] Michalski CW, Kleeff J, Wente MN, *et al*. Systematic review and meta-analysis of standard and extended lymphadenectomy in pancreaticoduodenectomy for pancreatic cancer. Br J Surg 2007;94:265–73.

[13] Jang JY, Kang MJ, Heo JS, *et al*. A prospective randomized controlled study comparing outcomes of standard resection and extended resection, including dissection of the nerve plexus and various lymph nodes, in patients with pancreatic head cancer. Ann Surg 2014;259:656–64.

[14] Chang ST, Jeffrey RB, Patel BN, *et al*. Preoperative multidetector CT Diagnosis of extrapancreatic perineural or duodenal invasion is associated with reduced postoperative survival after pancreaticoduodenectomy for pancreatic adenocarcinoma: preliminary experience and implications for patient care. Radiology 2016;281:816–25.

[15] Khristenko E, Shrainer I, Setdikova G, *et al*. Preoperative CT-based detection of extrapancreatic perineural invasion in pancreatic cancer. Sci Rep 2021;11:1800.

[16] Li J, Kang R, Tang D. Cellular and molecular mechanisms of perineural invasion of pancreatic ductal adenocarcinoma. Cancer Commun (Lond) 2021;41:642–60.

[17] Bakst RL, Wong RJ. Mechanisms of perineural invasion. J Neurol Surg B Skull Base 2016;77:96–106.

[18] Gao Z, Zong Q, Wang Y, *et al*. Laplacian salience-gated feature pyramid network for accurate liver vessel segmentation. IEEE Trans Med Imaging 2023;42:3059–68.

[19] Khan TM, Naqvi SS, Robles-Kelly A, *et al*. Retinal vessel segmentation via a Multi-resolution Contextual Network and adversarial learning. Neural Netw 2023;165:310–20.

[20] Bossuyt PM, Reitsma JB, Bruns DE, *et al*. STARD 2015: an updated list of essential items for reporting diagnostic accuracy studies. BMJ 2015;351:h5527.

[21] Collins GS, Reitsma JB, Altman DG, *et al*. Transparent reporting of a multivariable prediction model for individual prognosis or diagnosis (TRIPOD): the TRIPOD statement. BMJ 2015;350:g7594.

[22] Shi C, Siegelman SS, Kawamoto S, *et al*. Pancreatic duct stenosis secondary to small endocrine neoplasms: a manifestation of serotonin production? Radiology 2010;257:107–14.

[23] Watanabe H, Okada M, Kaji Y, *et al*. [New response evaluation criteria in solid tumours-revised RECIST guideline (version 1.1)]. Gan To Kagaku Ryoho 2009;36:2495–501.

[24] Guo X, Gao S, Yu J, *et al*. The imaging features of extrapancreatic perineural invasion (EPNI) in pancreatic CAncer : a comparative retrospective study. Pancreatology 2021;21:1516–23.

[25] Yi SQ, Miwa K, Ohta T, *et al*. Innervation of the pancreas from the perspective of perineural invasion of pancreatic cancer. Pancreas 2003;27:225–9.

[26] van der Walt S, Schonberger JL, Nunez-Iglesias J, *et al*. scikit-image: image processing in Python. PeerJ 2014;2:e453.

[27] Li W, Liu H, Qian W, *et al*. Hyperglycemia aggravates microenvironment hypoxia and promotes the metastatic ability of pancreatic cancer. Comput Struct Biotechnol J 2018;16:479–87.
[28] Yang YH, Liu JB, Gui Y, *et al*. Relationship between autophagy and perineural invasion, clinicopathological features, and prognosis in pancreatic cancer. World J Gastroenterol 2017;23:7232–41.
[29] Crippa S, Pergolini I, Javed AA, *et al*. Implications of perineural invasion on disease recurrence and survival after pancreatectomy for pancreatic head ductal adenocarcinoma. Ann Surg 2022;276:378–85.
[30] Bozkurt M, Eldem G, Bozbulut UB, *et al*. Factors affecting the response to Y-90 microsphere therapy in the cholangiocarcinoma patients. Radiol Med 2021;126:323–33.
[31] Nicolo E, Tarantino P, D'Ecclesiis O, *et al*. Baseline tumor size as prognostic index in patients with advanced solid tumors receiving experimental targeted agents. Oncologist 2024;29:75–83.
[32] Wahl RL, Jacene H, Kasamon Y, *et al*. From RECIST to PERCIST: Evolving Considerations for PET response criteria in solid tumors. J Nucl Med 2009;50(Suppl 1):122S–50S.
[33] Cha DE, Yu AT, Khajoueinejad N, *et al*. Perineural invasion of pancreatic ductal adenocarcinoma is associated with early recurrence after neoadjuvant therapy followed by resection. World J Surg 2023;47:1801–8.
[34] Karim MR, Islam T, Shajalal M, *et al*. Explainable AI for bioinformatics: methods, tools and applications. Brief Bioinform 2023;24:bbad236.
[35] Sufyan M, Shokat Z, Ashfaq UA. Artificial intelligence in cancer diagnosis and therapy: Current status and future perspective. Comput Biol Med 2023;165:107356.
[36] Huff DT, Weisman AJ, Jeraj R. Interpretation and visualization techniques for deep learning models in medical imaging. Phys Med Biol 2021;66:04TR01.
[37] Luchian A, Cepeda KT, Harwood R, *et al*. Quantifying acute kidney injury in an Ischaemia-Reperfusion Injury mouse model using deep-learning-based semantic segmentation in histology. Biol Open 2023;12:bio059988.
[38] Mahmoudi T, Kouzahkanan ZM, Radmard AR, *et al*. Segmentation of pancreatic ductal adenocarcinoma (PDAC) and surrounding vessels in CT images using deep convolutional neural networks and texture descriptors. Sci Rep 2022;12:3092.
[39] Li Q, Zhou Z, Chen Y, *et al*. Fully automated magnetic resonance imaging-based radiomics analysis for differentiating pancreatic adenosquamous carcinoma from pancreatic ductal adenocarcinoma. Abdom Radiol (NY) 2023;48:2074–84.
[40] Kaur H, Saini SK, Thakur N, *et al*. Survey of denoising, segmentation and classification of pancreatic cancer imaging. Curr Med Imaging 2024;20:e150523216892.
[41] Zhang Z, Tian H, Xu Z, *et al*. Application of a pyramid pooling Unet model with integrated attention mechanism and Inception module in pancreatic tumor segmentation. J Appl Clin Med Phys 2023;24:e14204.